



# Fast synthesis of highly crystallized LSX zeolite with boosted carbon dioxide hydrogenation activity

Mei Xiang<sup>a,b,1</sup>, Zhisheng Shi<sup>c,1</sup>, Linchang Tong<sup>a,1</sup>, Peng Li<sup>d</sup>, Xinpeng Zhang<sup>a</sup>, Zeying Wu<sup>a,e</sup>, Jirong Bai<sup>a</sup>, Wei Zhang<sup>a</sup>, Zhenwei Zhang<sup>a</sup>, Songyun Ma<sup>f</sup>, Yaoyao Deng<sup>a,\*</sup>, Jiancheng Zhou<sup>b,\*</sup>, Yaqiong Su<sup>d,\*</sup>

<sup>a</sup> Research Center of Secondary Resources and Environment, School of Chemical Engineering and Materials, Changzhou Institute of Technology, Xinbei District, Changzhou 213032, Jiangsu, PR China

<sup>b</sup> Department of Chemical Engineering, School of Chemistry and Chemical Engineering, Southeast University, Jiangning District, Nanjing 211189, Jiangsu, PR China

<sup>c</sup> School of Chemical and Environmental Engineering, Anhui Laboratory of Clean Energy Materials and Chemistry for Sustainable Conversion of Natural Resources, Anhui Polytechnic University, Jiujiang District, Wuhu 241000, Anhui, PR China

<sup>d</sup> School of Chemistry, Xi'an Key Laboratory of Sustainable Energy Materials Chemistry, State Key Laboratory of Electrical Insulation and Power Equipment, Xi'an Jiaotong University, Xi'an 710049, Shanxi, PR China

<sup>e</sup> Jiangsu Key Laboratory of Advanced Catalytic Materials and Technology, Changzhou University, 213164, China

<sup>f</sup> Institute of General Mechanics (IAM), RWTH Aachen University, Eilfschornsteinstraße 18, Aachen 52062, Germany

## ARTICLE INFO

### Keywords:

LSX zeolite catalyst  
Fast synthesis  
CO<sub>2</sub> hydrogenation  
100% methanol selectivity  
Reaction mechanism

## ABSTRACT

Fabrication of suitable zeolite-based multifunctional catalysts has been perceived as a potential method for CO<sub>2</sub> conversion to value-added chemicals and fuels. Thus, a highly crystallized LSX zeolite was prepared directly for the first time without aging and strong alkali sodium/potassium salt. Besides, the hierarchical structure was also successfully introduced by template-free method. The resulted LSX zeolite-based catalyst can significantly boost CO<sub>2</sub> hydrogenation with a preferential production of methanol (100% selectivity). This can be owing to the electron transfer between extra framework aluminum (EFAl) and ZnO species that drives the remarkable adsorption capability of CO<sub>2</sub> and the formate activation pathway. Furthermore, the highly dispersive Cu nanoparticles that interplay with zeolite host and ZnO species render convenient access to the activated CO<sub>2</sub>\* species for those dissociated H after their spillover. More importantly, an exceptional stability can also be obtained, indicating the promising prospect in practical and industrial application.

## 1. Introduction

Catalytic transformation of CO<sub>2</sub> with green H<sub>2</sub> to methanol has attracted both academic and industrial interest due to the vital role of CH<sub>3</sub>OH in energy storage, chemical synthesis, and thereby forming a closed carbon-fuel-cycle [1–4]. Hence, given the economic value and appealing environmental benefits, a number of efforts have been devoted to establishing an energy-efficient catalytic hydrogenation process of CO<sub>2</sub> for methanol synthesis, which proves the requirement for developing high-performance catalysts [5–7]. Besides, considering that the formation of methanol from CO<sub>2</sub> is actually an exothermic process and inevitably accompanied by the competitive reverse water-gas shift (RWGS) reaction, it is necessary for a desired catalyst doing well in

low-temperature activation of CO<sub>2</sub> in order to keep from equilibrium-limitation [8–10].

Among the widely reported CO<sub>2</sub> hydrogenation catalysts, copper-based catalysts are the most extensively investigated because of their less prone to over-reduced products (e.g., CH<sub>4</sub>) formation, especially the Cu/ZnO/Al<sub>2</sub>O<sub>3</sub> ternary catalyst that has been systematically studied and industrially used for synthesizing methanol from the syngas (CO and H<sub>2</sub>) [11–14]. However, except for methanol producing, Cu/ZnO/Al<sub>2</sub>O<sub>3</sub> also shows great enthusiasm for RWGS reaction, which is bound to negatively influence methanol selectivity. Besides, the sintering and deactivation of the Cu-based catalyst caused by water during CO<sub>2</sub> hydrogenation is another hard nut to crack [15–17]. What's more, both CO<sub>2</sub> conversion and CH<sub>3</sub>OH selectivity in CO<sub>2</sub> hydrogenation reactions

\* Corresponding authors.

E-mail addresses: [dengyy@czu.cn](mailto:dengyy@czu.cn) (Y. Deng), [jczhou@seu.edu.cn](mailto:jczhou@seu.edu.cn) (J. Zhou), [yqsu1989@xjtu.edu.cn](mailto:yqsu1989@xjtu.edu.cn) (Y. Su).

<sup>1</sup> These authors have contributed equally to this work.

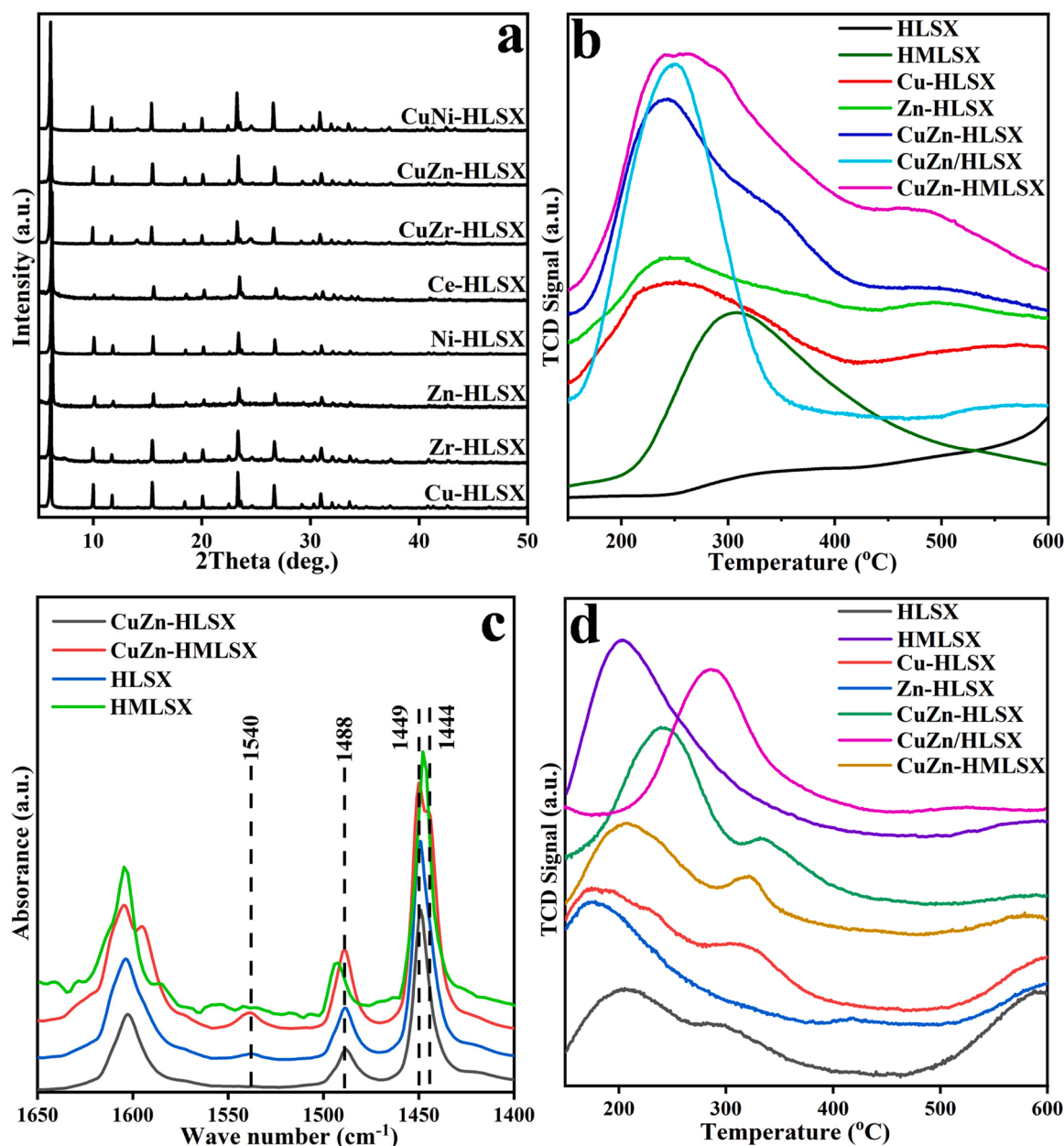


Fig. 1. (a) XRD patterns, (b) NH<sub>3</sub>-TPD profiles, (c) pyridine-FTIR spectra and (d) CO<sub>2</sub>-TPD profiles of the LSX-based catalyst samples.

strongly depend on the supports and promoters, of which the constructive roles they play in improving catalytic performance is still under debate [18–20]. Catalysts based on other metal oxides such as ZnO-ZrO<sub>2</sub>, CdZrO<sub>x</sub> and GaZrO<sub>x</sub> solid solution catalysts, and noble metals were then developed and perceived as alternatives to Cu-based catalysts, which enjoy fairly competitive power in terms of stability and resistance to sintering and poisoning [21–27]. Nevertheless, these catalysts still suffer from low catalytic efficiency and selectivity, indicating there remains challenges to rationally optimize different catalysts for exclusively selective transformation of CO<sub>2</sub> to specific chemicals.

Bifunctional catalysts composed of metal/metal oxides and zeolite/zeotype materials provide an alternative for hydrogenation reactions [28–32]. Series of zeolite-based catalysts have been reported and employed recently during CO<sub>2</sub> conversion process, demonstrating that combining the advantages of zeolites and metallic species is a wise move for efficiently producing desired products [33–35]. Particularly, the unique intra-pore spatial confinement effects and distinctive anchoring active metal species competence of zeolites is decisive not only in

promoting the selectivity toward target products, but also in improving the catalytic stability by restraining aggregation and deactivation.

The low-silica zeolite X (LSX) with typical FAU framework and Si/Al molar ration ranging from 1.0 to 1.1 has been certified to be noteworthy for its distinctive porous structure and intraskeletal cation distribution, remarkable ion-exchange capacity and fantastic thermal and thermal stability [36–39]. More importantly, the inherently high counter-ion concentration and surface area endows it with prominent adsorption capacity for CO<sub>2</sub>, which proves to be not only double than conventional X zeolite but also superior to many other reported zeolites [40–44]. Hence, in order to cater to the desired selectivity needs of CO<sub>2</sub> hydro-conversion, highly crystallized LSX zeolite was prepared in this work by a fascinating way, which proposed the synthesis strategy for the first time that successfully quitted the dependence on strong alkalinity and aging process. Besides, hierarchical LSX zeolite (MLSX) was also developed. When used for CO<sub>2</sub> hydrogenation reactions, a dramatic selectivity of methanol (100%) was obtained with 22.66% CO<sub>2</sub> being converted under relatively mild conditions (3.5 MPa, 200 °C and 2 h). In

**Table 1**

The physic-chemical properties of LSX-based catalysts.

Sample	C <sup>a</sup> (%)	Cu <sup>b</sup> (wt%)	Zn <sup>c</sup> (wt%)	d <sub>Cu</sub> <sup>d</sup> (%)	S <sub>BET</sub>	S <sub>micro</sub>	S <sub>meso</sub>	V <sub>micro</sub>	V <sub>meso</sub>	Pore <sup>e</sup> (nm)
HLSX	80.1				440.6	402.0	38.6	0.17	0.05	3.2
HMLSX	74.8				702.2	626.5	75.7	0.35	0.13	11.9
Cu-HLSX	82.3	1.04		34.0	682.2	641.3	40.8	0.25	0.04	3.9
Zn-HLSX	64.7		1.56		380.9	366.5	44.4	0.15	0.07	5.0
Zr-HLSX	71.3				457.2	428.9	28.3	0.15	0.01	3.1
Ni-HLSX	76.5				530.0	490.3	39.7	0.23	0.03	3.9
Ce-HLSX	69.8				450.0	420.6	29.4	0.16	0.03	3.8
CuZr-HLSX	70.7				426.6	398.1	28.8	0.14	0.01	2.9
CuNi-HLSX	74.2				420.8	393.1	27.7	0.17	0.02	3.4
CuCe-HLSX	70.3				402.6	362.9	39.7	0.18	0.04	4.2
CuZn-HLSX	73.6	1.36	0.89	60.1	499.1	450.6	48.6	0.15	0.10	4.9
CuZn/HLSX	79.0	2.38	3.04	31.2	418.7	371.6	47.1	0.14	0.04	4.0
CuZn-HMLSX	73.4	2.87	3.30	63.3	689.0	616.9	72.1	0.50	0.15	11.5

<sup>a</sup> Crystallinity calculated by Scherrer equation.<sup>b</sup> The actual Cu contents detected by ICP.<sup>c</sup> The actual Zn contents detected by ICP.<sup>d</sup> The dispersion of Cu determined by N<sub>2</sub>O-TPD.<sup>e</sup> The pore width calculated using desorption branch

situ DRIFT spectroscopy and DFT calculations were then employed to explore the possible reaction mechanism in detail.

## 2. Experimental methods

### 2.1. Catalyst preparation

The synthesis of LSX zeolite was carried out with a molar composition of 1.0 Al<sub>2</sub>O<sub>3</sub>: 2.2 SiO<sub>2</sub>: 5.6 Na<sub>2</sub>O: 122.0 H<sub>2</sub>O under hydrothermal condition. Firstly, 2.5 g sodium aluminate was dissolved in 20 mL deionized water. After continuous stirring for 10 min, 6.8 g sodium chloride was added into the resulted solution followed by further stirring for 10 min. Subsequently, the mixture composed of 5.7 mL aqueous water glass solution (SiO<sub>2</sub>/Na<sub>2</sub>O molar ratio:3.3, and density:1.38 g/cm<sup>3</sup>) and 8.5 mL deionized water was added and stirred for 30 min. The obtained gel was then transferred into a 50 mL stainless steel autoclave for crystallization at 100 °C for 6.0 h. The resulting product was filtered and washed to pH≈ 7 by deionized water before being dried at 105 °C for 12 h, followed by calcination at 450 °C for 4 h.

In order to introduce active metal species, an in-situ doping method was adopted, during which a certain amount of metal nitrates solution was directly added into the final synthesis gel mentioned above before it was transferred into stainless steel autoclave for crystallization. The obtained metal-containing zeolite was named M'-LSX and M'-MLSX, of which M' and M refer to metal species and hierarchical structure, respectively. The H-form samples (HLSX, HMLSX, M'-HLSX and M'-HMLSX) were obtained by NH<sub>4</sub><sup>+</sup> ion exchange, and the detailed preparation procedure is presented in [Supporting Information](#). Besides, CuZn-HZSM-5, CuZn-HBeta, CuZn-HSAPO-56, CuZn-HY and CuZn-HX were also prepared for comparison.

### 2.2. Catalyst evaluation

The CO<sub>2</sub> hydrogenation to methanol was conducted in a 50 mL high-pressure stainless-steel reactor with a magnetic stirrer. Initially, 0.05 g powdered catalyst that has been reduced by H<sub>2</sub> at 400 °C for 4 h was mixed with 5.0 mL 1,4-dioxane and then transferred into the reactor. The air in the reactor was beforehand displaced by CO<sub>2</sub>/H<sub>2</sub> forming gas. Subsequently, the 3.5 MPa of CO<sub>2</sub>/H<sub>2</sub> (1/3) was pumped into the reaction system and the reactor was heated to the desired temperature. After stabilization at reaction temperature for 10 min, the hydrogenation reaction was started with stirring at a specific speed of 400 rpm for a certain reaction time. The detail analysis of products can be seen in [Supporting Information](#).

## 3. Results and discussion

### 3.1. Synthesis of LSX zeolite

For improving traditional synthesis pathways that all could not be put into effect without the dependence of strongly alkaline NaOH, NaCl is attempted herein as the main sodium source and the impact of different Na/Al ratios on the LSX structure is explored after the Si/Al ratio was firstly determined at 1.1 (detailed discussion in [Supporting Information](#), Fig. S1a). According to the XRD patterns (Fig. S1b), the peak intensity increases positively with the Na/Al ratio, and the crystallinity of the resulted LSX zeolite reaches 100.00% when the Na/Al ratio is 6.25, which is contrary to the previous report that higher concentration of Na<sup>+</sup> tends to form LTA zeolite [45]. This can be ascribed to the structure-oriented effect of Cl<sup>-</sup> that can induce the nucleation of LSX zeolite and thus inhibit the formation of LTA zeolite. The investigated effect that followed was H<sub>2</sub>O/Al ratios and Si source (Fig. S1c and S1d), suggesting adopting a H<sub>2</sub>O/Al ratio of 122 and water glass as Si source is beneficial to high purity and crystallinity.

Up to now, aging treatment before crystallization has been regarded as the most widely and effective way to enhance the purity and crystallinity of the synthesized LSX zeolite. However, in this work, the aging contrast experiments reveals an interesting result. As can be seen in Fig. S2a, there is almost invisible difference in the peak intensity for the two samples. And the calculated crystallinity values are 97.4% and 93.1% for the LSX zeolite synthesized with aging process or not, which further confirms the feasibility and potential of employing the synthesis route without dependence on aging. Hence, inspired by this dramatic finding, investigations based on the non-aging process were carried out through comprehensive analyses discussed in [Supporting Information](#).

On top of this synthetic strategy, further study was carried out and fortunately, it was found that hierarchical structure could be directly introduced by adjusting inorganic species with the corresponding pore size distribution centered at 11.9 nm (see [Supporting Information](#)).

### 3.2. Physic-chemical properties of LSX-based catalysts

As evidenced in the XRD patterns of different LSX zeolite-based catalyst samples (Fig. 1a), FAU-type zeolite structure was presented without any impurity phase or distinctive metal-related diffraction peaks, indicating the highly dispersed metal atoms. Nevertheless, according to the crystallinity calculated by Scherrer equation [46] and shown in Table 1, Cu-HLSX is the only one with crystallinity higher than 80%. When introducing additional zinc species, the resulting bimetallic CuZn-HLSX catalyst gives obviously higher crystallinity (73.6%) than

**Table 2**The acid property and CO<sub>2</sub> adsorption capacity.

Sample	NH <sub>3</sub> -TPD		CO <sub>2</sub> -TPD	
	Desorption Peaks (°C)	Surface acidity (mmol/g)	Desorption Peaks (°C)	Quantity (mmol/g)
HLSX	178/470/540	0.30	206/290/585	0.061
HMLSX	333/420	0.32	203/587	0.078
Cu-HLSX	250/564	0.21	175/306	0.063
Zn-HLSX	248/369/490	0.19	180/418	0.042
CuZn-HLSX	240/345/500	0.28	242/331	0.087
CuZn/HLSX	250/562	0.25	140/287/525	0.073
CuZn-HMLSX	262/468	0.31	207/302/578	0.11
CuZn-HZSM-5	261/516	0.53	174/374/428	0.055
CuZn-HBeta	263/474	0.49	264/385/580	0.031
CuZn-HSAPO-56	303/523	0.22	156/385	0.028
CuZn/Al <sub>2</sub> O <sub>3</sub>	265/500	0.21	150/290/364	0.031
CuZn/SiO <sub>2</sub>	321	0.14	154/400	0.020
CuZn-HX	319	0.29	295	0.071
CuZn-HY	346	0.33	325	0.053

Zn-HLSX. This can be attributed to the specific Cu-Zn interaction that influenced their interplay with zeolite support, which is further confirmed by the textual properties shown in Table 1. The seriously decreased specific surface area of 380.9 m<sup>2</sup>/g for Zn-HLSX is definitely much lower than that of Cu-HLSX (682.2 m<sup>2</sup>/g) and CuZn-HLSX (499.1 m<sup>2</sup>/g), further proving the destructive action of zinc species on HLSX zeolite support and their fascinating interaction with those concomitant copper species. In addition, when compared with CuZn/HLSX prepared by impregnation method, the resulted higher metal loading, especially zinc contents (3.04 wt%), seems to be more detrimental to crystal structure with the specific surface area dropping severely to 418.7 m<sup>2</sup>/g though the crystallinity (79.0%) is little higher than that of CuZn-HLSX. While for CuZn-HLSX synthesized by in-situ doping, in spite of the inevitable metal loss that leads to low metal loading (Cu:1.36 wt%; Zn:0.89 wt%), the advantageous metal dispersion and active specific surface area highlight its application potential. When it comes to the hierarchical LSX zeolite-based catalyst, dramatic decline of the calculated crystallinity and specific surface area mainly happens during the protonation process, after which adding copper and zinc species do not make a considerable influence. More importantly, the introduced

hierarchical pores in HMLSX is definitely more tolerant of metal introduction than HLSX, which is also embodied in the less falling specific surface area and material crystallinity, as well as the improved metal dispersion. This manifests the catalytic superiority of introducing hierarchical structure that contributes to higher active surface area (689.0 m<sup>2</sup>/g) and wider pore size distribution (11.5 nm), enabling the promotion of zeolite hydrothermal stability and avoiding the pores and channels blockage from metal species.

Fig. 1b illustrates the NH<sub>3</sub>-TPD profiles of various LSX zeolite-based catalysts. One broad and distinctive peak in the range of 200–300 °C corresponding to weak acid sites is observed for all the supported catalysts doped with metal species. Besides, there is also observable ammonia desorption at high temperature range of 350–500 °C that is ascribed to strong acidic sites. While for the pristine HLSX, different desorption trend appears with three conspicuous peaks at 325, 505 and 620 °C that are due to moderately and strongly bound NH<sub>3</sub>, respectively. Furthermore, when combined with the actual total amount of acid sites (mmol·g<sup>-1</sup>) presented in Table 2, it is noteworthy that the incorporation of Cu or Zn species into HLSX support inevitably leads to dramatical reduction of NH<sub>3</sub> desorption amount from 0.30 mmol/g to 0.21 or 0.19 mmol/g, respectively. However, for CuZn-HLSX, the acidity loss is less severe than that of Cu-HLSX or Zn-HLSX, reconfirming the presence of an interesting interaction between Cu and Zn species that can adjust their interplay with HLSX support. But it seems that the preparation method can make a difference to their interaction according to the acidity comparison between CuZn-HLSX and CuZn/HLSX, where the latter shows nearly 0.03 mmol/g worse than the former. Apart from the samples mentioned above that are all based on HLSX, CuZn-HMLSX with two main desorption temperature of 255 and 470 °C exhibits increased both acid amounts (0.31 mmol·g<sup>-1</sup>) and strength, which can be attributed to the introduced hierarchical structure that benefits the exposure of more acid sites and improves the interaction between active metal species and zeolite support. For better comparison, several common catalyst supports with various structure were adopted and the corresponding catalysts acid properties are also given (Fig. 2a), of which two main desorption peaks signifying medium (250–350 °C) and strong (>350 °C) acidic sites are observed. It is no doubt that CuZn-HZSM-5, CuZn-HBeta and CuZn-HY are the three most acidic samples with the total amount of acid sites apparently higher than that of others (Table 2). Even though being not at par with the first three samples, CuZn-HMLSX, CuZn-HLSX and CuZn-HX in the second echelon still have obvious advantages comparing with CuZn-HSAPO-56, CuZn/Al<sub>2</sub>O<sub>3</sub> and CuZn/SiO<sub>2</sub>.

Fig. 2b presents the pyridine-FTIR spectra to identify the Brønsted and Lewis acid sites (BAS and LAS) types on catalysts. The main

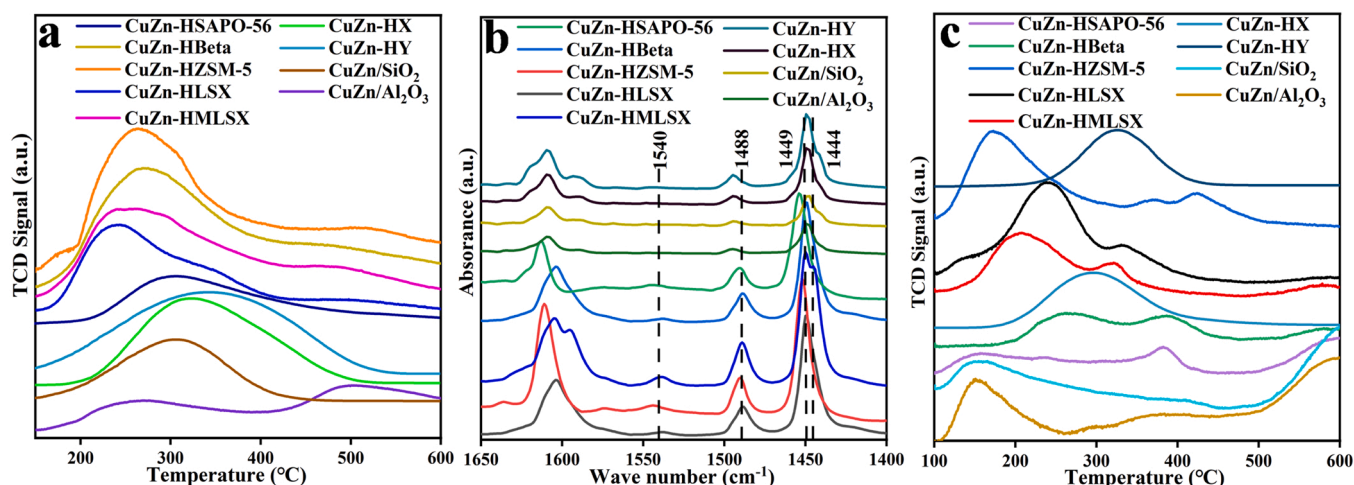
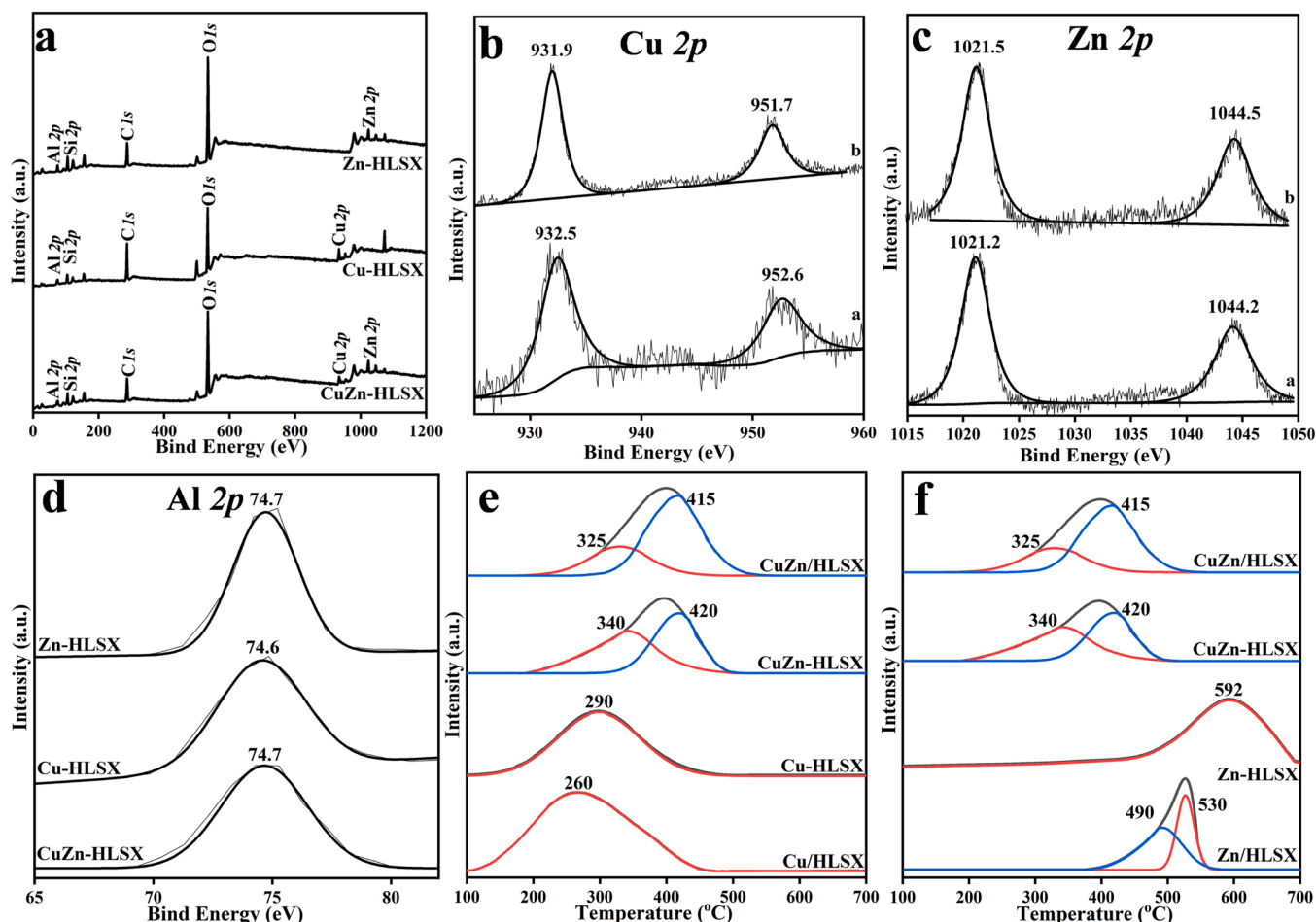


Fig. 2. (a) NH<sub>3</sub>-TPD profiles, (b) pyridine-FTIR spectra and (c) CO<sub>2</sub>-TPD profiles of CuZn-based catalyst samples.





**Fig. 3.** XPS spectra for (a) survey spectra patterns; (b) Cu 2p for a) CuZn-HLSX and b) Cu-HLSX samples; (c) Zn 2p for a) CuZn-HLSX and b) Zn-HLSX samples; (d) Al 2p; and H<sub>2</sub>-TPR profiles ((e) and (f)) of HLSX-based catalyst samples.

adsorption bands at 1540 cm<sup>-1</sup>, 1488 cm<sup>-1</sup>, and 1449 cm<sup>-1</sup> can be assigned to BAS, BAS+LAS, and LAS, respectively [47]. Compared with pristine HLSX, the bands of BAS and BAS+LAS shift toward lower wave number with the introduction of hierarchical structure, whereas the peak amplitude of LAS heightens substantially. The same trend occurs with the incorporation of metal species. Remarkably, for CuZn-HLSX, the BAS peak at 1540 cm<sup>-1</sup> almost disappears, leaving the LAS dominates the acid sites. As a matter of fact, it has been confirmed by previous studies that the introduction of finely dispersed Cu species is able to make contribution to creating the strong Lewis acid sites [48], with which the result of both pyridine-FTIR spectra and NH<sub>3</sub>-TPD in this work is highly consistent. Moreover, this can also be owing to those introduced hierarchical pores that resulted in the improved dispersion of Cu species, which further brings the relative LAS increased. Besides, combined with the comparison of

the total surface acidity from NH<sub>3</sub>-TPD results between CuZn-HLSX and Cu-HLSX, the extremely prominent presence of LAS on CuZn-HLSX is also closely related to the existed Zn species, which can function and perform effectively by their interaction with HLSX zeolite and Cu species. Thus, the evolution of acidity over HLSX-based catalysts could be due to the exposure and distribution of the catalytic active sites, as well as the interactions among different species. For other CuZn-based catalysts samples with various acid strength, the similar distribution of acid types that feature predominant Lewis acid property is noticeable in Fig. 2b.

CO<sub>2</sub> adsorption is generally regarded as a prerequisite for its effectively catalytic conversion, so that CO<sub>2</sub>-TPD was employed to establish the surface adsorption of CO<sub>2</sub> on the reduced HLSX-based and other

CuZn catalysts, and their desorption profiles are shown in Fig. 1d and Fig. 2c. As a whole, the desorption temperature lower than 150 °C is related to weakly basic sites that is derived from surface OH groups. And the peaks at the temperature range of 150–450 °C are assigned to medium-strength basic sites and associated with the desorption of bidentate species. Higher temperature peaks (> 450 °C) are corresponding to the strong basic sites. Here, the desorption of CO<sub>2</sub> on the HLSX-based catalysts mostly takes place in the temperature range of 150–450 °C, indicating almost all have moderate basic sites and the CO<sub>2</sub> molecular can be effectively activated in this range. Notable is, compared with pure HLSX, the Cu appearing as a separate existence on the HLSX shows minimal increased CO<sub>2</sub> adsorption, which drops sharply on Zn-HLSX. While for the samples with a combination of both the Cu and Zn species, the desorption peaks increase obviously. The CO<sub>2</sub> adsorption capability listed in Table 2 presents the follow order: CuZn-HLSX (0.11 mmol·g<sup>-1</sup>) > CuZn-HLSX (0.087 mmol·g<sup>-1</sup>) > HLSX (0.078 mmol·g<sup>-1</sup>) > CuZn/HLSX (0.073 mmol·g<sup>-1</sup>) > Cu-HLSX (0.063 mmol·g<sup>-1</sup>) > HLSX (0.061 mmol·g<sup>-1</sup>) > Zn-HLSX (0.042 mmol·g<sup>-1</sup>). Thus, it could be deduced that CO<sub>2</sub> molecules are possibly not adsorbed on copper species. Besides, in view of the clearly rising CO<sub>2</sub> adsorption quantity on those bimetallic catalyst samples, it follows that the aggressive effect from zinc species on LSX zeolite largely improves. That is to say, if ruling out the structural damage from zinc species on LSX zeolite framework that leads to declined CO<sub>2</sub> adsorption, it is plausible that ZnOx sites combined with the zeolite support took on mainly CO<sub>2</sub> adsorption and activation. Comparatively, even though most of the other bimetallic catalysts also show similar base strength distribution (Fig. 2c), their total CO<sub>2</sub> adsorption capacity were all

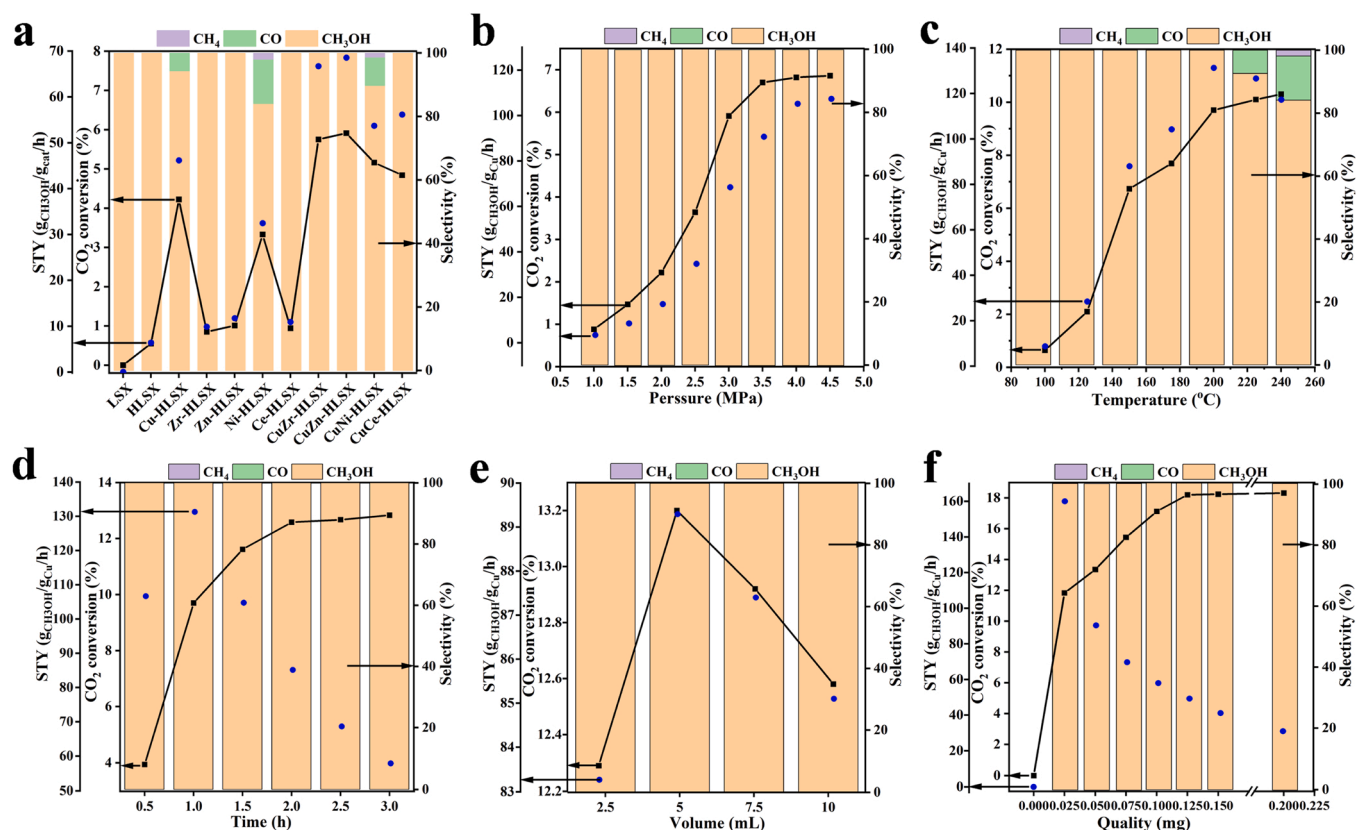


Fig. 4. CO<sub>2</sub> conversion, methanol selectivity and STY on various catalysts under different reaction conditions.

inferior to CuZn-HMLSX, CuZn-HLSX and CuZn/HLSX (as shown in Table 2).

In order to probe into the surface composition and electronic state details of active sites on the LSX-based catalysts, XPS experiments of the in-situ reduced catalysts were performed (Figs. 3a–3d). For Cu-HLSX, two characteristic peaks at 931.9 and 951.7 eV assigned to Cu 2p<sub>3/2</sub> and Cu 2p<sub>1/2</sub>, respectively, can be observed without any satellite peaks existing, fully demonstrating that the presence of Cu<sup>0</sup> species and those CuO having been completely reduced to the metallic form. When it comes to the CuZn-HLSX, a red shift of the Cu 2p peak positions to 932.5 and 952.6 eV happens, indicating the possibility of specific interaction between Cu and Zn species being formed. The Zn 2p core level spectra of CuZn-HLSX shown in Fig. 3c with two strong peaks appearing at 1021.2 and 1044.2 eV are attributed to Zn 2p<sub>3/2</sub> and Zn 2p<sub>1/2</sub>, respectively. According to the standard XPS spectrum of Zn species, the binding energy of 2p<sub>3/2</sub> for Zn<sup>0</sup> and ZnO is 1021.7 and 1021.3 eV, respectively [49]. Clearly, the peak position at 1021.1 eV of ZnO species for CuZn-HLSX is mostly identical to that of the standard ZnO XPS spectrum, suggesting that nearly all the zinc species on the CuZn-HLSX exist in the form of Zn (II). While for Zn-HLSX, it is ambiguous whether Zn (II) or Zn (0) dominated the existence form of zinc species because the binding energy of 2p<sub>3/2</sub> at 1021.5 eV has the same gap (0.2 eV) with that at 1021.7 eV and 1021.3 eV from the standard XPS spectrum. It is worth noting that both of these two characteristic peaks positions in CuZn-HLSX shift to lower binding energy compared with Zn-HLSX, which can be explained by the possible electron transfer between Zn species and Cu species, as well as the HLSX zeolite support. The XPS spectra of Al 2p is also investigated to further illuminate the role of zinc species on the CuZn-HLSX catalyst sample. As shown in Fig. 3d, the binding energy at 74.7 eV for both CuZn-HLSX and Zn-HLSX is marginally higher than that for Cu-HLSX with a proximate value (74.8 eV) to the standard spectra of extra-framework aluminum (74.6 eV). In other words, there could be some special interaction

between zinc species and those extra-framework aluminum from zeolite support. Thus, combined with the appreciably decreases binding energy of Zn 2p, it can be deduced that the electron transfer from extra-framework aluminum to ZnO species on the CuZn-HLSX does exist. For the sake of further identifying their interactions and accessing their reduction behavior on the zeolite support, H<sub>2</sub>-TPR was employed. It can be found that even though with similar Cu loading, the reduction of Cu species on the Cu-HLSX begins at higher temperature than that of Cu/HLSX, indicating that the in situ doped Cu species is more hardly reduced owing to their stronger interaction with zeolite support. Besides, when compared with the other two bimetallic samples, the onset reduction temperature is apparently lower without the addition of ZnO<sub>x</sub>, offering further grounds for the interaction between Cu and Zn species within the HLSX zeolite framework. What's more, other than Cu-HLSX with only one broad peak being detected around 290 °C that is assigned to the well-dispersed CuO species reduction, it is interesting to note that the reduction peak of CuZn-HLSX shows a red shift to 340 °C with the intensity heightened, also demonstrating the existence of specific interaction produced by addition of Zn species that limits CuO to be reduced. On the other side, for the Zn-HLSX sample, it exhibits only one broad reduction peak at 595 °C with the starting reduction temperature obviously higher than 400 °C. Similarly, the reduction of Zn/HLSX also concentrates in the high temperature region (490 and 530 °C) and its corresponding starting point visibly exceeds 400 °C. Thus, the confusion about the existence form of zinc species on the Zn-HLSX from the XPS spectra discussed above can be removed. The reduction process operated at 400 °C in this work is insufficient for Zn<sup>0</sup> species coming into being. Besides, the lower reduction temperature of the surface zinc species on CuZn/HLSX (415 °C) and CuZn-HLSX (420 °C) indicates that the coexistence with Cu species can lead to easier reduction of ZnO<sub>x</sub> species and strongly evidence it deserves to put much stock in their interaction.

### 3.3. Catalytic activity in CO<sub>2</sub> hydrogenation reactions

The performance of various catalysts was examined in 1,4-dioxane at 100–240 °C and 1.0–4.5 MPa after elimination of internal and external diffusion (see Supporting Information, Fig. S6). Before the CO<sub>2</sub> hydrogenation experiments, all the catalysts were preprocessed for activation in the H<sub>2</sub> flow at 400 °C for 4 h. It has been reported that Cu-based catalysts with well-ordered 3D channels for transforming CO<sub>2</sub> into methanol are good at controlling the particle size and regulating the interaction between catalytic active sites and reactants (H<sub>2</sub> and CO<sub>2</sub>), resulting in optimized performance [50]. Surely, in this work, among series of LSX zeolite-based catalysts, CuZn-HLSX catalyst proves itself can realize double advantage effectively under rather mild condition (Fig. 4a), which outperforms others in the highest CO<sub>2</sub> conversion (5.9%) and methanol selectivity (100%). Besides, it is notable that the CO<sub>2</sub> hydrogenation activity is positively associated with the bimetallic component and acidity. As can be seen in Fig. 4a, only when the Na, K-type LSX is protonated to HLSX, does the CO<sub>2</sub> conversion begin. Even though the activity is quite low with merely 0.55% CO<sub>2</sub> being converted, the methanol selectivity of 100% is remarkable enough to affirm the importance of catalyst acidity and the strong methanol directed-synthesis ability of HLSX zeolite. However, this conspicuous hydrogenation selectivity is likely to be influenced by metal introduction. In Fig. 4a, copper and nickel species are the two most active factors that stimulate CO<sub>2</sub> conversion rising above 3.0% but at the cost of forming CO and methane. As a result, it is inevitable for the CuNi-HLSX catalyst being able to enhance the hydrogenation activity and simultaneously foster side reactions, making for a 5.2% conversion of CO<sub>2</sub> and yielding methanol as low as 46.3%. Interestingly, although the methanol selectivity of CuNi-HLSX (89.7%) is clearly lower than that of Cu-HLSX (94.3%), it is still 5.7% higher than that of Ni-HLSX, indicating the advantage of bimetallic component focuses not only on maximizing their hydrogenation activity but also on improving the undesired tendency to CO and methane. Likewise, the combination of Cu and Zn species with HLSX generates delightful performance in CO<sub>2</sub> hydrogenation, obtaining the highest CO<sub>2</sub> conversion without any CO and methane formed. Among those single metal catalysts, Zr-HLSX is the least effective with just 0.85% CO<sub>2</sub> being converted to methanol, while the assembly with copper species leads to more than 5 times increasing of CO<sub>2</sub> conversion (5.8%). It is worth noting that apart from CuNi-HLSX, all of the other three bimetallic catalysts that share the same support and copper participant have strong preference for methanol formation, which offers further grounds for interaction between different metal species that can directly affect the correspondingly catalytic activity.

According to the Le Chatelier's principle, the reaction pressure is also of great significance for CO<sub>2</sub> hydrogenation to methanol, which is a reaction proceeded with decreasing number of molecules. Hence, the higher CO<sub>2</sub> conversion is expected, the higher pressure is needed. Furthermore, increasing the reaction pressure is beneficial to reinforcing the contact between the reactants and catalysts. As shown in Fig. 4b, both the CO<sub>2</sub> conversion and STY value monotonically increase with reaction pressure. And their rapid growth tends to slow down until the pressure is raised greater than 3.5 MPa. It should be noted that no matter what the reaction pressure is, the methanol selectivity (100%) keeps unchanged. Therefore, considering the cost and demand for practical industrial applications, it is better for the operation pressure being as low as possible. Herein, the desired CO<sub>2</sub> conversion and methanol selectivity can be obtained under a relatively mild reaction pressure of 3.5 MPa.

Due to the exothermal nature of CO<sub>2</sub> hydrogenation to methanol, the CO<sub>2</sub> conversion and methanol selectivity of this thermodynamically controlled process present contradictory requirements for reaction temperature. Fig. 4c shows the influence of temperature on the catalytic performance over CuZn-HLSX. The CO<sub>2</sub> conversion increases from 0.6% to 10.3% when the reaction temperature ranges from 100 °C to 240 °C, while the perfect methanol selectivity is not maintained after further

**Table 3**

CO<sub>2</sub> hydrogenation over different catalysts (Reaction conditions: catalyst 0.15 g, 1,4-dioxane 5 mL, 3.5 MPa, 200 °C, 2 h and 400 rpm).

Catalyst	C <sup>a</sup> (%)	S <sup>b</sup> <sub>1</sub> (%)	S <sup>c</sup> <sub>2</sub> (%)	S <sup>d</sup> <sub>3</sub> (%)	STY/ g <sub>CH<sub>3</sub>OH</sub> •g <sub>Cu</sub> <sup>-1</sup> •h <sup>-1</sup>	TOF
CuZn-HLSX	18.2	100.0	0.0	0.0	41.1	21.2
CuZn/HLSX	12.4	100.0	0.0	0.0	27.9	14.4
CuZn- HMLSX	22.7	100.0	0.0	0.0	51.1	26.4
CuZn-HZSM- 5	14.9	93.0	5.3	1.8	31.2	17.1
CuZn- HBETA	15.7	95.2	4.8	0.0	33.6	16.1
CuZn- HSPA0-56	10.0	93.6	6.4	0.0	21.1	10.9
CuZn-HX	8.2	100.0	0.0	0.0	18.5	9.5
CuZn-HY	9.5	82.2	17.8	0.0	17.7	9.1
CuZn/Al <sub>2</sub> O <sub>3</sub>	6.2	80.6	19.4	0.0	11.2	5.8
CuZn/SiO <sub>2</sub>	3.3	73.0	27.0	0.0	5.5	2.8

<sup>a</sup> Conversion of CO<sub>2</sub>.

<sup>b</sup> Selectivity of CH<sub>3</sub>OH.

<sup>c</sup> Selectivity of CO.

<sup>d</sup> Selectivity of CH<sub>4</sub>.

increasing the temperature higher than 200 °C. That is to say, there is a seesaw effect between CO<sub>2</sub> conversion and methanol selectivity in a certain temperature range. This can be owing to the presence of competitive reverse water gas shift (rWGS) reaction that is endothermic and will be promoted to form CO at high temperature, thus leading to the reduction of methanol selectivity. In this work, CO comes into being as the reaction temperature rises to 225 °C, and then its selectivity further increases to 14.0% at 240 °C accompanied by slight formation of methane. Notably, it is also at this temperature do the STY values decrease. Hence, in order to effectively suppress the rWGS reaction and activate CO<sub>2</sub> as much as possible, a reaction temperature of 200 °C is more suitable for methanol formation.

Fig. 4d displays the catalytic performance of 0.05 g CuZn-HLSX catalyst at 200 °C and 3.5 MPa as a function of time. It is obvious that the CO<sub>2</sub> conversion increases but the methanol selectivity completely unaffected with increasing of reaction time. However, from the point of STY, it seems that 2 h reaction time is feat enough for a maximum formation of methanol on a specified amount of catalyst. And further prolonging the time will facilitate CO<sub>2</sub> conversion to reach a plateau and correspondingly bring about the decline of methanol forming rate, which is reflected in the drastically falling STY values from 131.2 to 57.9. Therefore, a reaction time of 2 h is chosen with the conversion being as high as 12.6% and modest STY values (85.1 g<sub>CH<sub>3</sub>OH</sub>•g<sub>Cu</sub><sup>-1</sup>•h<sup>-1</sup>). Subsequently, the effect of solvent volume on catalytic performance was evaluated and the result is shown in Fig. 4e. As can be seen, variation of the 1,4-dioxane volume from 2.5 mL to 10.0 mL has no significant impact on the methanol selectivity, but does make difference in the CO<sub>2</sub> conversion. Either lower or higher volume than 5.0 mL gives rise to markedly decrease of methanol formation, which may be related to the limited access to the catalytic active centers for reactants. Hence, it is decided to employ 5.0 mL as the desired 1,4-dioxane use level for further optimization.

As for the dosage of catalyst, the blank control trial was firstly carried out with no CO<sub>2</sub> transformation at all, suggesting the requirement of catalyst existence. Indeed, it can be seen from Fig. 4f that even using a trace amount of CuZn-HLSX can greatly improve the CO<sub>2</sub> hydrogenation activity, which comes up directly with further addition of the catalyst. And the methanol selectivity of 100% can also be always kept. Thus, taking into account the CO<sub>2</sub> conversion, methanol selectivity and the STY value, catalyst content of 0.15 g is adopted for the subsequent research.

In order to understand the role of the support that is essential to rational design of CO<sub>2</sub> hydrogenation catalysts, ten CuZn-based samples



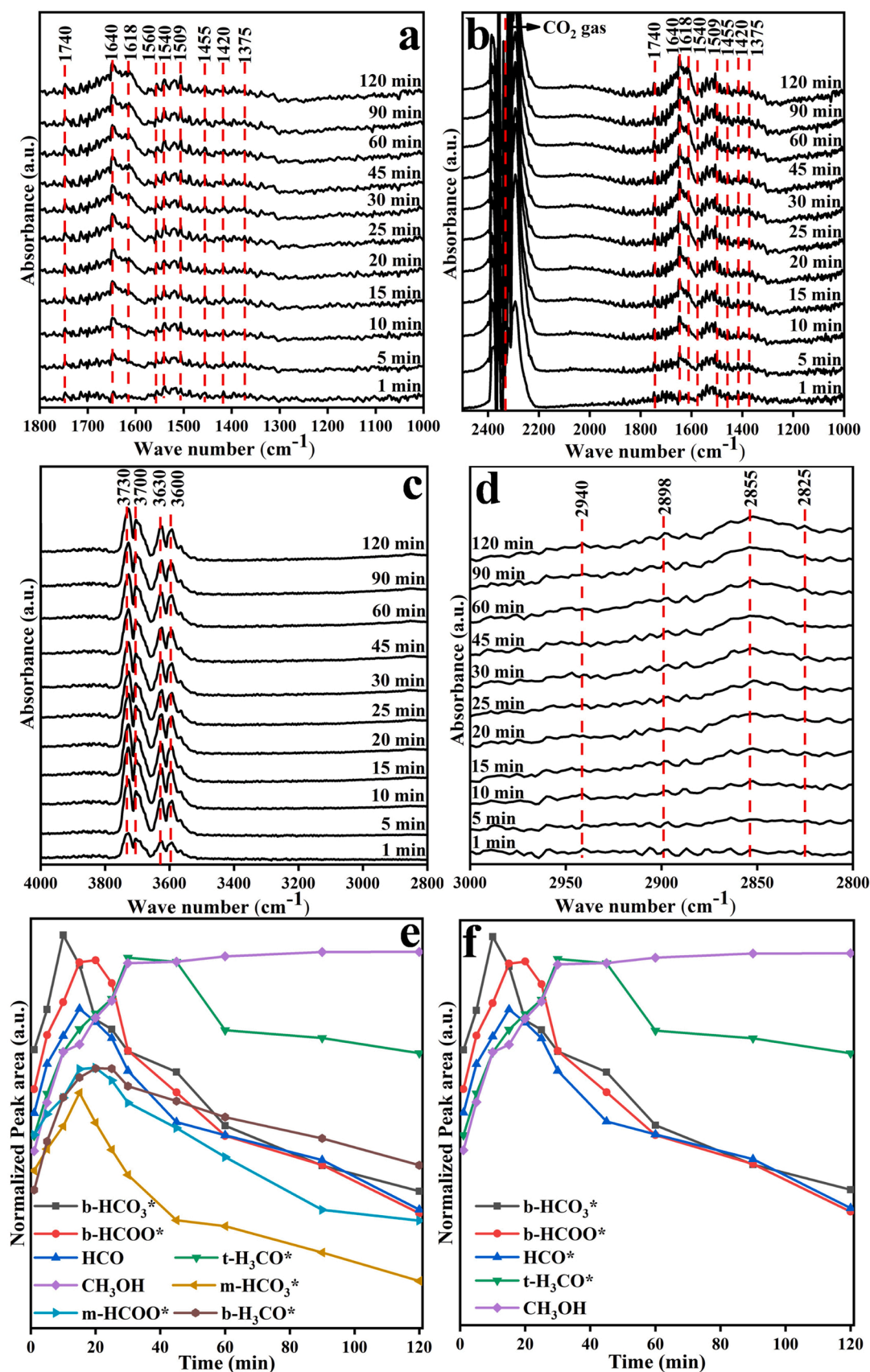


Fig. 5. *In situ* DRFT spectra obtained on CuZn-HLSX (a)-(d); and the kinetic study of the intermediate products (e) and (f).



were prepared and used in batch reactions of methanol synthesis. As shown in Table 3, performance of those catalysts varies considerably in activity and selectivity, among which the CuZn-HLSX, CuZn-HMLSX and CuZn-HBeta catalysts obtained the largest methanol space time yield of 41.1, 51.1 and 33.6  $\text{g}_{\text{CH}_3\text{OH}}/\text{g}_{\text{Cu}}\cdot\text{h}^{-1}$ , respectively. While referring to the methanol selectivity, the outstanding CuZn-HBeta sample suffers an eclipse with some of the converted  $\text{CO}_2$  being set aside to form the unexpected CO. Similarly, CuZn-HZSM-5, a catalyst composed of the most popular zeolite support (ZSM-5), did well in promoting  $\text{CO}_2$  conversion, but paled in comparison with methanol yield. For CuZn-HY and CuZn-HSPA0-56 catalysts that also contain two common supports, in cases where  $\text{CO}_2$  conversion is the only consideration, the catalytic performance is fair to middling. Unfortunately, the obvious CO affinity makes their weakness in methanol selectivity (82.2% and 93.6%) fully come to light. CuZn-HX catalyst which consists of another familiar zeolite support X sharing the same basic framework with LSX, though is uncompetitive in highly efficient activation of  $\text{CO}_2$ , it deserves great expectations on synthesizing methanol with a 100% selectivity. The two industrial CuZn-based catalysts (CuZn/ $\text{Al}_2\text{O}_3$  and CuZn/ $\text{SiO}_2$ ) tests under the optimized reaction conditions was performed poorly and found to be ineffective to yield methanol with the  $\text{CO}_2$  conversion being far behind and affording significant amounts of CO byproduct. It should be noted that CuZn/HLSX prepared by impregnation method also proves itself to be a good candidate for methanol formation, whereas the  $\text{CO}_2$  conversion is still 5.9% lower than that of CuZn-HLSX. In general, the reactivity of  $\text{CO}_2$  hydrogenation to methanol follows the order: CuZn-HMLSX (C:22.7%, S:100%) > CuZn-HLSX (C:18.2%, S:100%) > CuZn-HBeta (C:15.7%, S:95.2%) > CuZn-HZSM-5 (C:14.9%, S:93.0%) > CuZn/HLSX (C:12.7%, S:100%) > CuZn-HSAPO-56 (C:10.0%, S:93.6%) > CuZn-HX (C:8.0%, S:100%) > CuZn-HY (C:9.5%, S:82.2%) > CuZn/ $\text{Al}_2\text{O}_3$  (C:6.2%, S:80.6%) > CuZn/ $\text{SiO}_2$  (C:3.3%, S:73.0%), which is closely related to multifactor functioning mainly including active metal dispersion and interaction, acidity and acid strength,  $\text{CO}_2$  adsorption and activation capacity, the framework and pore structure of support. First of all, with the same HLSX zeolite support, CuZn-HLSX shows a decided advantage over CuZn/HLSX in converting  $\text{CO}_2$  to methanol though the actual metal contents of the latter are about twice more than that of the former, which has a lot to do with the marked metal dispersion difference ( $D_{\text{CuZn-HLSX}}$ :60.1%;  $D_{\text{CuZn/HLSX}}$ :31.2%). For the most outstanding candidate, CuZn-HMLSX is endowed with the greatest strength of being introduced hierarchical structure that dramatically benefits the access of reactant molecules ( $\text{CO}_2$  and  $\text{H}_2$ ) to active sites, and promotes the interaction between metal species and zeolite support, as well as the requisite  $\text{CO}_2$  adsorbing capability. Besides, when compared with the three most common and medium strong acid zeolite catalysts CuZn-HBeta, CuZn-HZSM-5 and CuZn-HY, regardless of  $\text{CO}_2$  conversion, those moderately acidic LSX zeolite-based catalysts undoubtedly hold overwhelming superiority in methanol selectivity (100%). The comparison between CuZn-HX and CuZn-HY makes this more convinced. On the other hand, if the catalyst acidity is not strong enough, such as CuZn/ $\text{Al}_2\text{O}_3$  and CuZn/ $\text{SiO}_2$ , it is insufficient to satisfy the needs of  $\text{CO}_2$  adsorption and activation with high efficiency, and more importantly, methanol formation will also be significantly inhibited. In order to further obtain a better insight into the reasons behind different reactivity, the relationship between  $\text{CO}_2$  conversion, methanol STY and the amount of desorbed  $\text{NH}_3$  or  $\text{CO}_2$  over various catalysts was displayed in Fig. S7. Obviously, CuZn-HLSX and CuZn-HMLSX gave the largest amount of desorbed  $\text{CO}_2$  among all the catalysts, thus corresponding to the highest  $\text{CO}_2$  conversion and methanol yield. Especially, for the four catalyst samples CuZn-HX, CuZn/HLSX, CuZn-HLSX and CuZn-HLSX that are prepared with the same FAU type of zeolite support, it is apparent that the corresponding  $\text{CO}_2$  conversion increased monotonously with increasing the amount of desorbed  $\text{CO}_2$ . As is also clear from Fig. S7, when the amount of desorbed  $\text{NH}_3$  increases, both the  $\text{CO}_2$  conversion and methanol STY increase at first, reach their first peak at CuZn-HLSX, and then fluctuate at CuZn-HX,

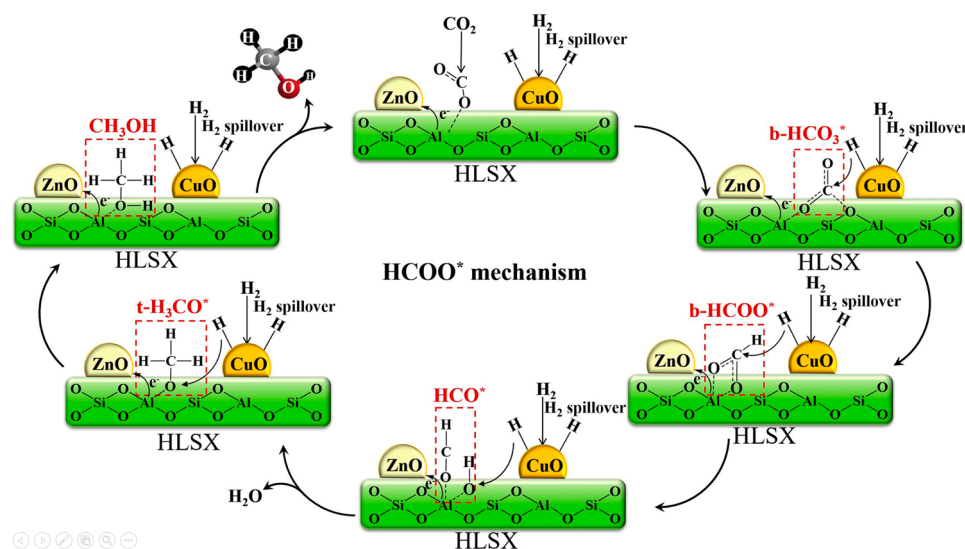
after which their maximum values are obtained at CuZn-HMLSX. CuZn-HZSM-5 gives the largest amount desorbed  $\text{NH}_3$  but a medium catalytic performance, suggesting that high acidity is not good for improving  $\text{CO}_2$  conversion and methanol selectivity. In addition, the fluctuation of the  $\text{CO}_2$  conversion and methanol STY reconfirms that acidity and acid strength,  $\text{CO}_2$  adsorption and activation capacity play leading roles in  $\text{CO}_2$  hydrogenation to methanol, but not the only influencing factors.

The catalytic performance of CuZn-HLSX and CuZn-HMLSX for  $\text{CO}_2$  hydrogenation to methanol is not only superior to those catalysts mentioned above, but also preeminent among various catalysts reported previously. As can be seen from Table S3, for most of the catalysts, a good balance between  $\text{CO}_2$  conversion and methanol selectivity is always absent. Firstly, for the three catalysts with a 100% methanol selectivity, aside from their strong dependence on the existence of Mn as promoter, the comparatively low  $\text{CO}_2$  conversion (< 10%) makes them undesirable in methanol formation. For the relatively better one prepared by noble metal Pd, even though there are certain advantages in catalytic activity, the high cost and severe reaction conditions bring it obvious disadvantages.

### 3.4. The $\text{CO}_2$ hydrogenation mechanism

*In situ* DRFT experiments were performed to monitor the  $\text{CO}_2$  hydrogenation process and thus identify the possible intermediates species on the catalyst surface during the reaction. Fig. 5, Fig. S8 and Fig. S9 illustrate *in situ* DRFT spectra obtained on CuZn-HLSX, Cu-HLSX and HLSX with  $\text{HCO}_3^*$ ,  $\text{HCOO}^*$ , and  $\text{H}_3\text{CO}^*$  species being identified as the main intermediates in all cases. And precisely, these catalysts samples also show quite similar bands, indicating the same intermediates and adsorption sites. Table S4 lists the peak assignments based on the control experiments, among which those at 1509, 1640, 3600 and 3630  $\text{cm}^{-1}$  are attributed to the presence of adsorbed bidentate bicarbonate ( $\text{bi-HCO}_3^*$ ) related to hydroxyls [51–53]. For  $\text{HCOO}^*$  species, the bands are located at 1540, 1560  $\text{cm}^{-1}$  ( $\text{m-HCOO}^*$ ) and 1375, 1618  $\text{cm}^{-1}$  ( $\text{bi-HCOO}^*$ ) [54,55]. Others at 1455, 2825, 2898 and 2940  $\text{cm}^{-1}$  are assigned to the  $\text{H}_3\text{CO}^*$  ( $\text{t-H}_3\text{CO}^*$  and  $\text{b-H}_3\text{CO}^*$ ) species. Moreover, the adsorption band belongs with formyl ( $\text{HCO}^*$ ) species at 1740  $\text{cm}^{-1}$  can also be observed. And the bands at 2855, 3730, 3700  $\text{cm}^{-1}$  are owing to the formed isolated OH groups of methanol [56,57]. Fortunately, neither gas CO nor adsorbed CO, as well as methane, is detected on both HLSX and CuZn-HLSX, which is distinguished from Cu-HLSX with weak adsorption band of undesired gaseous CO species (2160  $\text{cm}^{-1}$ ) being observed (Fig. S9). This demonstrates that the  $\text{CO}_2$  hydrogenation to methanol on HLSX and CuZn-HLSX is more likely to abide by the same  $\text{HCOO}^*$ -intermediated reaction pathway. It is noteworthy that *in situ* DRFT experiments with no use of solvent also elucidate the availability of catalyst in gas phase for  $\text{CO}_2$  hydrogenation to produce methanol.

On the other hand, by comparing the *in situ* DRFT spectra of HLSX and Cu-HLSX, not only the band intensity of  $\text{bi-HCO}_3^*$  (at 3600 and 3630  $\text{cm}^{-1}$ ) and  $\text{bi-HCOO}^*$  (at 1618  $\text{cm}^{-1}$ ) increased apparently, but also did new adsorption peaks at 1540 and 1455  $\text{cm}^{-1}$  that are bound to  $\text{m-HCOO}^*$  and  $\text{t-H}_3\text{CO}^*$  intermediates emerge [58], illustrating the necessity of  $\text{Cu}^0$  species that endows catalyst with correspondingly indispensable  $\text{H}_2$  adsorption and dissociation capacity. And the detected gaseous CO band at 2160  $\text{cm}^{-1}$  for Cu-HLSX is coincident with the catalytic activity test result (Fig. 5a), which intuitively shows there existed a small amount of CO. Further comparison between these two catalyst samples mentioned above and CuZn-HLSX witnessed that the  $\text{CO}_2$  adsorption quantity is substantially more increased along with a series of relatively hydrogenated intermediates being produced due to the synergistic function of  $\text{Cu}^0$ , ZnO species and the Lewis acid sites on the HLSX zeolite. Indeed, it has been proved that there is definite charge transfer from Cu and Lewis acid center to ZnO species, leading to the enhanced  $\text{H}_2$  adsorption and dissociation capacity of  $\text{Cu}^0$  species, and resulting in the Lewis acid center being more electron-deficient to



**Scheme 1.** The proposed mechanism for CO<sub>2</sub> hydrogenation on CuZn-HLSX.

improve the performance of CO<sub>2</sub> adsorption-activation.

For ease of correlating the intermediates buildup/decay with time and going into their dynamic behavior, the semi-quantitative evolution methodology is adopted, which is based on the peak deconvolution of the corresponding IR band for CuZn-HLSX catalyst sample [59]. As can be seen in Fig. 5e and f, the bands corresponding to bi-HCO<sub>3</sub><sup>\*</sup> species can be observed as soon as the feed gas (CO<sub>2</sub> + H<sub>2</sub>) is exposed into the system, and its growth reaches the peak very fast at the beginning 10 min, demonstrating that bi-HCO<sub>3</sub><sup>\*</sup> is most probably to be the first CO<sub>2</sub> activated intermediate and its hydrogenation is instantaneous. Along with bi-HCO<sub>3</sub><sup>\*</sup> comes the substantial increase of bi-HCOO<sup>\*</sup>, which appears from 1 to 15 min and is followed by the HCO<sup>\*</sup> species with similar generation. Just like bi-HCO<sub>3</sub><sup>\*</sup>, bi-HCOO<sup>\*</sup> and HCO<sup>\*</sup> intermediates that all experienced the fastest growth in the first 10 min, t-H<sub>3</sub>CO<sup>\*</sup> species also show the maximum growth rate during this time period, after which the increase slowdown emerges. In addition, according to the peak intensity, it just takes 20 min for the surface bi-HCOO<sup>\*</sup> species to reach a steady peak state on CuZn-HLSX, while for t-H<sub>3</sub>CO<sup>\*</sup> much more time (~30 min) is needed, which proves that t-H<sub>3</sub>CO<sup>\*</sup> can be derived from bi-HCOO<sup>\*</sup> hydrogenation. It is worth noting that before the t-H<sub>3</sub>CO<sup>\*</sup> concentration gradually approaches an equilibrium, a sharp reduction from 45 to 60 min happens, and it is right around this time do the generation of methanol almost stop. Besides, it is visualized the rising tendency of methanol keeps pace with that of t-H<sub>3</sub>CO<sup>\*</sup> species prior to the consumable intermediate on the decrease. Moreover, compared with Cu-HLSX and HLSX showing trace amount of t-H<sub>3</sub>CO<sup>\*</sup> species, the t-H<sub>3</sub>CO<sup>\*</sup> formed on the CuZn-HLSX is relative active and well-marked. Thus, taking the higher STY of CH<sub>3</sub>OH obtained on the CuZn-HLSX catalyst into account, it can be assumed that the generated t-H<sub>3</sub>CO<sup>\*</sup> species have dominated methanol synthesis during CO<sub>2</sub> hydrogenation. In fact, as is generally acknowledged, HCOO<sup>\*</sup> and H<sub>3</sub>CO<sup>\*</sup> are exactly the most significant intermediate species for methanol synthesis during CO<sub>2</sub> hydrogenation, and the formation of HCOO<sup>\*</sup> is a kinetically fast process while its subsequent hydrogenation process to produce H<sub>3</sub>CO<sup>\*</sup> is relatively difficult, which greatly depends on the catalyst hydrogenation ability. Herein, considering the fact that there are only weak peaks of HCOO<sup>\*</sup> observed over Cu-HLSX and HLSX catalysts, their disadvantage in obtaining high STY of CH<sub>3</sub>OH can be explained. On the contrary, for CuZn-HLSX, with the enhanced dispersion of Cu nanoparticles and their interaction with both ZnO and LSX support, not only the initial appearance and growth of bi-HCO<sub>3</sub><sup>\*</sup>, bi-HCOO<sup>\*</sup>, HCO<sup>\*</sup> and t-H<sub>3</sub>CO<sup>\*</sup> species are promoted, but also are closely related to each other. And more importantly, they are directly

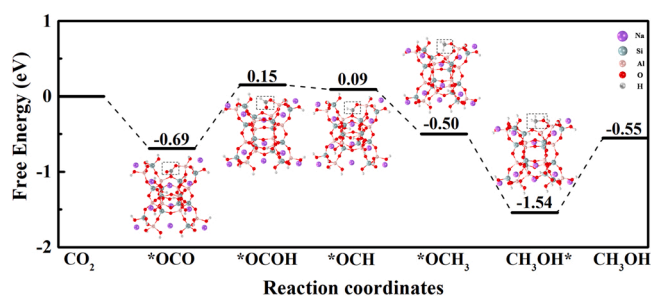


**Fig. 6.** Free energy diagram for comparing the intermediates involved in CO<sub>2</sub> hydrogenation to methanol via the formate pathway.

associated with CO<sub>2</sub> activation and hydro-conversion to methanol. While for m-HCO<sub>3</sub><sup>\*</sup>, m-HCOO<sup>\*</sup> and b-H<sub>3</sub>CO<sup>\*</sup> species, their corresponding peak intensity is significantly lower than that of methanol all along, illustrating they are not much involved and do not play a leading role in CO<sub>2</sub> transformation.

Hence, the possible pathway of CO<sub>2</sub> activation and hydrogenation to methanol on CuZn-HLSX catalyst can be proposed. As is shown in Scheme 1, with active H<sup>\*</sup> spillover from surface Cu<sup>0</sup> species and being coupled with the bridged oxygen of Al<sup>3+</sup>-O-Zn<sup>n+</sup> (1 < n < 2) site, CO<sub>2</sub> was firstly adsorbed and activated on the electron-deficient Lewis acid center of HLSX zeolite and mainly form bi-HCO<sub>3</sub><sup>\*</sup> intermediate, which depleted fast to produce bi-HCOO<sup>\*</sup> and m-HCOO<sup>\*</sup> species. Even though both the two formate species are able to be hydrogenated into the target product (CH<sub>3</sub>OH), bi-HCOO<sup>\*</sup> seems to play a decisive role in the subsequent hydrogenation process and thus make major contribution to the increase of methanol concentration, during which HCO<sup>\*</sup> and t-H<sub>3</sub>CO<sup>\*</sup> are the two most important intermediates that dominate further hydrogenation. While for b-H<sub>3</sub>CO<sup>\*</sup> coming from the hydrogenation of m-HCOO<sup>\*</sup> species, it also took part in methanol formation but with limited capacity.

To shed light on the mechanism proposed above and rationalize the prominent catalytic performance of CuZn-HLSX for methanol formation, density functional theory (DFT) calculations were carried out, and the potential energy surface is shown in Fig. 6. The nearby CO<sub>2</sub> gas molecule was firstly adsorbed on the defective Al centers and then connected to the adjacent and bridged O atom to form a circular structure of Al-O-C-O. What followed was the generation of \*OCOH through a highly endergonic step, by 0.84 eV. Notably, herein, the O atom of the \*OCOH

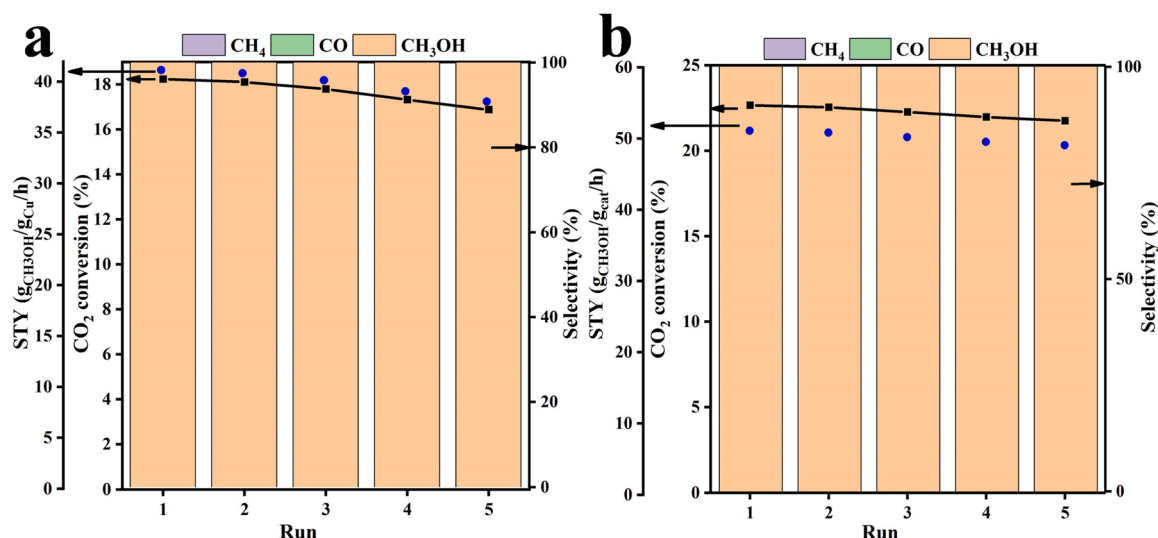


Fig. 7. Catalytic stability test of Cu-HLSX (a) and (b) Cu-HMLSX. Reaction condition: 0.15 g catalyst, 5 mL 1,4-dioxane, 3.5 MPa, 200 °C, 2 h and 500 rpm.

intermediate can bond with the close-by H<sub>2</sub> to produce a gaseous water molecule with a little heat release (0.06 eV). After the free gaseous H<sub>2</sub>O left the catalyst surface, the remained O-C-H would be adsorbed on the electron-deficient Al center and linked to the bridged O atom, leading to the formation of unstable Al-O-CH-O. Whereafter, a continued hydrogenation of Al-O-CH-O occurred, leading to the formation of Al-O-CH<sub>3</sub>. Then, along with the energy release (1.04 eV), the further hydrogenation product CH<sub>3</sub>OH is obtained, and its subsequent desorption costs energy of 0.99 eV. The results demonstrate that the rate determining step for CO<sub>2</sub> hydrogenation to methanol is the \*OCOH formation with comparatively low energy uphill (0.84 eV). Hence, we propose that the CO<sub>2</sub> hydrogenation can take place over the Al sites of zeolites.

### 3.5. Catalyst stability

Considering the indispensable role of catalyst stability and reusability, catalyst recycling experiments were carried out, before which the catalysts were recovered through centrifugation, filtration, washing, drying, calcination and reduction. After five experimental runs, the results showed that both the CO<sub>2</sub> conversion and CH<sub>3</sub>OH STY obtained on CuZn-HLSX present slight decrease (Fig. 7a). Similarly, for CuZn-HMLSX, the CO<sub>2</sub> hydrogenation remains the high methanol selectivity and conversion, which is obviously superior to those for CuZn-HLSX (Fig. 7b). This can be attributed to the hierarchical structure and higher active specific surface area that endow CuZn-HMLSX with more outstanding heat endurance. Subsequently, the used CuZn-HLSX and CuZn-HMLSX catalysts were characterized through XRD, IR, UV-vis and TGA technologies (Fig. S10). The XRD patterns of the two used catalyst samples demonstrate that the structure of CuZn-HLSX and CuZn-HMLSX is well reserved (Fig. S10a). In addition, the similar FTIR and UV-vis spectra of fresh and used catalysts also indicate the structure integrity is not apparently under threat during the extension use, which can be owing to their highly active specific surface area, high metal dispersion and appropriate interaction between Cu<sup>0</sup>, ZnO species and LSX zeolite. Moreover, the coke and carbon deposits were evaluated by means of thermogravimetric analyses (Fig. S10d). For the used CuZn-HLSX and CuZn-HMLSX samples, the total weight loss are 1.21 wt% and 1.06 wt%, respectively, and mainly occurs near 150 °C and 380 °C, indicating there is no evident coke and carbon deposits. In a word, according to the cycling test, it is clearly that CuZn-HLSX and CuZn-HMLSX can keep an exceptional stability during the CO<sub>2</sub> hydrogenation, indicating the great potential of this catalyst sample in practical and industrial application.

## 4. Conclusion

In conclusion, a facile synthesis of highly crystallized LSX zeolite was reported for the first neither relying on aging process nor binding with potassium source and strong alkali. Subsequently, a series of LSX zeolite-based catalysts were developed for hydrogenation of carbon dioxide, during which a preferential production of methanol (100% selectivity) was obtained with a formation rate of 51.1 g<sub>CH<sub>3</sub>OH</sub>■g<sub>Cu</sub><sup>-1</sup>■h<sup>-1</sup> under relatively mild reaction conditions (3.5 MPa, 200 °C). Experiments combined with comprehensive analyses reveal that the electron-deficient Lewis acid center and their interaction with ZnO species and the well dispersed Cu nanoparticles over CuZn-based LSX zeolite catalysts enhance the adsorption of CO<sub>2</sub> and the dissociation of H<sub>2</sub>. Thus, the dissociated H spillover and is endowed access to the activated CO<sub>2</sub> \* species, which facilitates the transformation of the resulted intermediated HCOO\* to CH<sub>3</sub>O\* and finally improves the formation of methanol.

### CRedit authorship contribution statement

**Mei Xiang:** Methodology, Data analysis, Investigation, Writing – original draft. **Zhisheng Shi:** Investigation, Writing – review & editing, Funding acquisition. **Linchang Tong:** Methodology, Investigation, Characterization analysis. **Peng Li:** Theoretical calculation, Formal analysis. **Xinpeng Zhang:** Formal analysis. **Zeyang Wu:** Writing – review & editing, Formal analysis. **Jirong Bai:** Investigation, Characterization analysis, Formal analysis. **Wei Zhang:** Investigation, Formal analysis. **Zhenwei Zhang:** Investigation, Formal analysis. **Songyun Ma:** Investigation, Writing – review & editing, Formal analysis. **Yaoyao Deng:** Conceptualization, Investigation, Funding acquisition. **Jiancheng Zhou:** Resources, Writing – review & editing. **Yaqiong Su:** Conceptualization, Resources, Writing – review & editing, Funding acquisition.

### Declaration of Competing Interest

The authors declare that they have no known competing financial interests or personal relationships that could have appeared to influence the work reported in this paper.

### Data availability

No data was used for the research described in the article.



## Acknowledgements

The authors thank the National Natural Science Foundation of China (No. 22208032), the Natural Science Foundation of the Jiangsu Higher Education Institutions of China (No. 20KJB530006, 20KJB150044), Science and Technology Foundation of Changzhou (No. CJ20200042), the Natural Science Foundation of the Higher Education Institutions of Anhui Province (No. KJ2020A0371), Jiangsu Key Laboratory of Advanced Catalytic Materials and Technology (No. BM2012110), the Foundation of Anhui Laboratory of Clean Energy Materials and Chemistry for Sustainable Conversion of Natural Resources (No. LCECSC-12), and the Research Start-up Foundation of Anhui Polytechnic University (No. 2020YQQ016). Y. Su acknowledges the “Young Talent Support Plan” of Xi'an Jiaotong University. Supercomputing facilities were provided by Hefei Advanced Computing Center.

## Authors' contributions

The manuscript was written through contributions of all authors. All authors have given approval to the final version of the manuscript.

## Appendix A. Supporting information

Supplementary data associated with this article can be found in the online version at [doi:10.1016/j.apcatb.2023.122576](https://doi.org/10.1016/j.apcatb.2023.122576).

## References

- [1] S. Navarro, M. Virginie, J. Bonin, M. Robert, W. Robert, Y. Andrei, Highlights and challenges in the selective reduction of carbon dioxide to methanol, *Nat. Rev. Chem.* 5 (2021) 564–579.
- [2] X. Jiang, X. Nie, X. Guo, C. Song, J.G. Chen, Recent advances in carbon dioxide hydrogenation to methanol via heterogeneous catalysis, *Chem. Rev.* 120 (2020) 7984–8034.
- [3] C.L. Mathis, J. Geary, Y. Ardon, M.S. Reese, M.A. Philliber, R.T. Vanderlinden, C. T. Saouma, Thermodynamic analysis of metal-ligand cooperativity of PNP Ru complexes: implications for CO<sub>2</sub> hydrogenation to methanol and catalyst inhibition, *J. Am. Chem. Soc.* 141 (2019) 14317–14328.
- [4] Y. Guo, X. Guo, C. Song, X.H. Han, H.Y. Liu, Z.K. Zhao, Capsule-Structured Copper-Zinc Catalyst for Highly Efficient Hydrogenation of Carbon Dioxide to Methanol, *ChemSusChem* 12 (2019) 4916–4926.
- [5] Y. Kuwahara, T. Mihogi, K. Hamahara, K. Kazuki, K. Hisayoshi, Y. Hiromi, A quasi-stable molybdenum sub-oxide with abundant oxygen vacancies that promotes CO<sub>2</sub> hydrogenation to methanol, *Chem. Sci.* 12 (2021) 9902–9915.
- [6] M.D. Burkart, N. Hazari, C.L. Tway, E.L. Zeitler, Opportunities and challenges for catalysis in carbon dioxide utilization, *ACS Catal.* 9 (2019) 7937–7956.
- [7] M. Mureddu, F. Ferrara, A. Pettinau, Highly efficient CuO/ZnO/ZrO<sub>2</sub>@SBA-15 nanocatalysts for methanol synthesis from the catalytic hydrogenation of CO<sub>2</sub>, *Appl. Catal. B: Environ.* 258 (2019), 117941.
- [8] D.X. Yang, Q.G. Zhu, C.J. Chen, H.Z. Liu, M. Zhi, Selective electroreduction of carbon dioxide to methanol on copper selenide nanocatalysts, *Nat. Commun.* 677 (2019).
- [9] D. Adekoya, M. Tahir, N. Aishah, S. Amin, Recent trends in photocatalytic materials for reduction of carbon dioxide to methanol, *Renew. Sustain. Energy Rev.* 116 (2019), 109389.
- [10] P. Maksimov, A. Laari, V. Ruuskanen, T. Koiranen, J. Ahola, Methanol synthesis through sorption enhanced carbon dioxide hydrogenation, *Chem. Eng. J.* 418 (2021), 129290.
- [11] W. Wang, Z. Qu, L. Song, F. Qiang, Probing into the multifunctional role of copper species and reaction pathway on copper-cerium-zirconium catalysts for CO<sub>2</sub> hydrogenation to methanol using high pressure in situ DRIFTS, *J. Catal.* 382 (2020) 129–140.
- [12] B.S. Xaba, A.S. Mahomed, H.B. Friedrich, The effect of CO<sub>2</sub> and H<sub>2</sub> adsorption strength and capacity on the performance of Ga and Zr modified Cu-Zn catalysts for CO<sub>2</sub> hydrogenation to methanol, *J. Environ. Chem. Eng.* 9 (2021), 104834.
- [13] D. Gómez, C. Candia, R. Jiménez, A. Karelavic, Isotopic transient kinetic analysis of CO<sub>2</sub> hydrogenation to methanol on Cu/SiO<sub>2</sub> promoted by Ga and Zn, *J. Catal.* 406 (2022) 96–106.
- [14] K. Li, J.G. Chen, CO<sub>2</sub> hydrogenation to methanol over ZrO<sub>2</sub>-containing catalysts: insights into ZrO<sub>2</sub> induced synergy, *ACS Catal.* 9 (2019) 7840–7861.
- [15] W. Wang, Z. Qu, L. Song, Q. Fu, CO<sub>2</sub> hydrogenation to methanol over Cu/CeO<sub>2</sub> and Cu/ZrO<sub>2</sub> catalysts: tuning methanol selectivity via metal-support interaction, *J. Energy Chem.* 40 (2020) 22–30.
- [16] J. Coreo, C.W. Lopes, L. Liu, S. Jose, A. Giovanni, B. Solson, R.T. Patricia, Cu-Ga<sup>3+</sup>-doped wurtzite ZnO interface as driving force for enhanced methanol production in co-precipitated Cu/ZnO/Ga<sub>2</sub>O<sub>3</sub> catalysts, *J. Catal.* 407 (2022) 149–161.
- [17] I. Abbas, H. Kim, C.H. Shin, S. Yoond, D.J. Kwang, Differences in bifunctionality of ZnO and ZrO<sub>2</sub> in Cu/ZnO/ZrO<sub>2</sub>/Al<sub>2</sub>O<sub>3</sub> catalysts in hydrogenation of carbon oxides for methanol synthesis, *Appl. Catal. B: Environ.* 258 (2019), 117971.
- [18] X. Yu, L. Yang, Y. Xuan, L.L. Xiang, K. Zhang, Solar-driven low-temperature reforming of methanol into hydrogen via synergetic photo-and thermocatalysis, *Nano Energy* 84 (2021), 105953.
- [19] J. Wang, G. Zhang, J. Zhu, X.B. Zhang, F.S. Ding, A.F. Zhang, X.W. Guo, C.S. Song, CO<sub>2</sub> hydrogenation to methanol over In<sub>2</sub>O<sub>3</sub>-based catalysts: from mechanism to catalyst development, *ACS Catal.* 11 (2021) 1406–1423.
- [20] S. Dang, B. Qin, Y. Yang, H. Wang, Y. Sun, Rationally designed indium oxide catalysts for CO<sub>2</sub> hydrogenation to methanol with high activity and selectivity, *Sci. Adv.* 6 (2020) 2060.
- [21] Z. Han, C. Tang, F. Sha, S. Tang, J.J. Wang, C. Li, CO<sub>2</sub> hydrogenation to methanol on ZnO-ZrO<sub>2</sub> solid solution catalysts with ordered mesoporous structure, *J. Catal.* 396 (2021) 242–250.
- [22] M. Mikhail, D.P. Costa, J. Amouroux, S. Cavadias, T. Michael, M.E. Gálvez, O. Stéphanie, Tailoring physicochemical and electrical properties of Ni/CeZrO<sub>x</sub> doped catalysts for high efficiency of plasma catalytic CO<sub>2</sub> methanation, *Appl. Catal. B: Environ.* 294 (2021), 120233.
- [23] F. Sha, C. Tang, S. Tang, Q.N. Wang, Z. Han, J.J. Wang, C. Li, The promoting role of Ga in ZnZrO<sub>x</sub> solid solution catalyst for CO<sub>2</sub> hydrogenation to methanol, *J. Catal.* 404 (2021) 383–392.
- [24] M. Kosari, U. Anjum, S. Xi, M. Alvin, H. Lim, M.S. Abdul, A.J. Raj, M. Sergey, B. Armando, C.Z. Hua, Revamping SiO<sub>2</sub> spheres by core-shell porosity endowment to construct a maze-like nanoreactor for enhanced catalysis in CO<sub>2</sub> hydrogenation to methanol, *Adv. Funct. Mater.* 31 (2021) 2102896.
- [25] H. Zhou, Z. Chen, A.V. López, L. Erwin, T. Athanasia, E. Willinger, A. Denis, D. Mance, K. Agnieszka, F. Donat, M. Paula, C.V. Aleix, C. Copéret, A. Fedorov, R. Christoph, Engineering the Cu/MoO<sub>2</sub>CT<sub>x</sub> (MXene) interface to drive CO<sub>2</sub> hydrogenation to methanol, *Nat. Catal.* 4 (2021) 860–871.
- [26] Y. Wang, S. Kattel, W. Gao, K.Z. Li, P. Liu, G. Jing, H. Wang, Exploring the ternary interactions in Cu-ZnO-ZrO<sub>2</sub> catalysts for efficient CO<sub>2</sub> hydrogenation to methanol, *Nat. Commun.* 10 (2019) 1–10.
- [27] J. Lopes, A.E. Bresciani, K.M. Carvalho, L.A. Kulay, R. Alves, Multi-criteria decision approach to select carbon dioxide and hydrogen sources as potential raw materials for the production of chemicals, *Renew. Sustain. Energy Rev.* 151 (2021).
- [28] W. Yue, Y. Li, W. Wei, J. Jiang, J. Caro, A. Huang, Highly selective CO<sub>2</sub> conversion to methanol in a bi-functional zeolite catalytic membrane reactor, *Angew. Chem.* 133 (2021) 18437–18442.
- [29] W.G. Cui, Y.T. Li, L. Yu, H.B. Zhang, T.L. Hu, Zeolite-encapsulated ultrasmall Cu/ZnO<sub>x</sub> nanoparticles for the hydrogenation of CO<sub>2</sub> to methanol, *ACS Appl. Mater. Interfaces* 13 (2021) 18693–18703.
- [30] S. Wang, T. Wu, J. Lin, J. Tian, Y.S. Ji, P. Yan, S.R. Yan, M.H. Qiao, H.L. Xu, B. N. Zong, FeK on 3D grapheme-zeolite tandem catalyst with high efficiency and versatility in direct CO<sub>2</sub> conversion to aromatics, *ACS Sustain. Chem. Eng.* 7 (2019) 17825–17833.
- [31] F. Huang, M. Peng, Y.L. Chen, X.B. Cai, X.T. Qin, N. Wang, D.Q. Xiao, L. Jin, G. Q. Wang, X.D. Wen, H.Y. Liu, D. Ma, Low-Temperature acetylene semi-hydrogenation over the Pd<sub>1</sub>-Cu<sub>1</sub> dual-atom catalyst, *J. Am. Chem. Soc.* 144 (2022) 18485–18493.
- [32] F. Huang, Y.C. Deng, Y.L. Chen, X.B. Cai, M. Peng, Z.M. Jia, J.L. Xie, D.Q. Xiao, X. D. Wen, N. Wang, Z. Jiang, H.Y. Liu, D. Ma, Anchoring Cu<sub>1</sub> species over nanodiamond-graphene for semi-hydrogenation of acetylene, *Nat. Commun.* 10 (2019) 4431.
- [33] X. Fang, H. Jia, B. Zhang, N. Ying, Y.S. Li, Y. Wang, S. Li, D. Tao, L.Y. Liu, A novel in situ grown Cu-ZnO-ZrO<sub>2</sub>/HZSM-5 hybrid catalyst for CO<sub>2</sub> hydrogenation to liquid fuels of methanol and DME, *J. Environ. Chem. Eng.* 9 (2021), 105299.
- [34] J. Wei, R. Yao, Y. Han, Q.J. Ge, J. Sun, Towards the development of the emerging process of CO<sub>2</sub> heterogeneous hydrogenation into high-value unsaturated heavy hydrocarbons, *Chem. Soc. Rev.* 50 (2021) 10764–10805.
- [35] Q. Zhang, J. Yu, A. Corma, Applications of zeolites to C1 chemistry: recent advances, challenges, and opportunities, *Adv. Mater.* 32 (2020) 2002927.
- [36] S.F. Ezzahra, B. Achiou, M. Ouammou, B. Mohamed, A. Younsi, E. Rhazi, Electrochemical sensor based on low silica X zeolite modified carbon paste for carbaryl determination, *J. Adv. Res.* (2017) 669–676.
- [37] Y. Lee, H. H. Lee, R.L. Dong, T.J. Shin, J.Y. Choi, C.C. Kao, Cation-dependent compression behavior in low-silica zeolite-X, *J. Am. Chem. Soc.* 129 (2007) 4888–4889.
- [38] M.G. José, I. Montes, E. Díez, A. Rodríguez, Mesoporous low silica X (MLSX) zeolite: mesoporosity in loewenstein limit, *Microporous Mesoporous Mater.* 330 (2022), 111618.
- [39] F. Wolf, H. Furtig, E. Lemnitz, Process for direct synthesis of sodium and potassium containing zeolite A, US 4534947 A (1985).
- [40] R. Kodasma, J. Ferosmo, A. Sanna, Li-LSX-zeolite evaluation for post-combustion CO<sub>2</sub> capture, *Chem. Eng. J.* 358 (2019) 1351–1362.
- [41] X. Yang, F.E. Epipegang, J.B. Li, Y.W. Wei, Y.S. Liu, R.T. Yang, Sr-LSX zeolite for air separation, *Chem. Eng. J.* 362 (2019) 482–486.
- [42] A.A. Leonova, M.S. Melgunov, Alteration of adsorption selectivity of LSX Zeolite in Li<sup>+</sup> and H<sup>+</sup> forms towards CO<sub>2</sub> and N<sub>2</sub>O, *Catal. Sustain. Energy* 4 (2017) 31–35.
- [43] S.J. Chen, M. Zhu, Y. Fu, Y.X. Huang, Z.C. Tao, W.L. Li, Using 13X, LiX, and LiPdAgX zeolites for CO<sub>2</sub> capture from post-combustion flue gas, *Appl. Energy* 191 (2017) 87–98.
- [44] N.R. Stuckert, R.T. Yang, CO<sub>2</sub> capture from the atmosphere and simultaneous concentration using zeolites and amine-grafted SBA-15, *Environ. Sci. Technol.* 45 (2011) 10257–10264.



- [45] J. Warzywoda, R.W. Thompson, Synthesis of zeolite A in the Na/K system and the effect of seeding, *Zeolites* 11 (1991) 577–582.
- [46] D. Akolekar, C. Alan, F.H. Russell, The transformation of kaolin to low-silica X zeolite, *Zeolites* 6 (1997) 359–365.
- [47] Q.J. Yu, J.Z. Li, C.C. Wei, Z. Shu, S.T. Xu, Z.M. Liu, Role of ball milling during Cs/X catalyst preparation and effects on catalytic performance in side-chain alkylation of toluene with methanol, *Chin. J. Catal.* 41 (2020) 1268–1278.
- [48] J. Klinowski, J.M. Thomas, C.A. Fyfe, G.C. Gobbi, Monitoring of structural changes accompanying ultrastabilization of faujasitic zeolite catalysts, *Nature* 296 (1982) 533–536.
- [49] M.C. Biesinger, W.M.L. Leo, A.R. Gerson, R.C. Smart, Resolving surface chemical states in XPS analysis of first row transition metals, oxides and hydroxides: Sc, Ti, V, Cu and Zn, *Appl. Surf. Sci.* 257 (2010) 887–898.
- [50] M. Kosari, U. Anjum, S.B. Xi, A.M.H. Lim, A.M. Seayad, E.A.J. Raj, S.M. Kozlov, A. Borgna, H.C. Zeng, Revamping SiO<sub>2</sub> spheres by core-shell porosity endowment to construct a mazelike nanoreactor for enhanced catalysis in CO<sub>2</sub> hydrogenation to methanol, *Adv. Funct. Mater.* 31 (2021) 2102896.
- [51] Y. Yan, R.J. Wong, Z.R. Ma, F. Donat, S.B. Xi, S. Saqline, Q.W.H. Fan, Y.H. Du, A. Borgna, Q. He, C.R. Müller, W. Chen, A.A. Lapkin, W. Liu, CO<sub>2</sub> hydrogenation to methanol on tungsten-doped Cu/CeO<sub>2</sub> catalyst, *Appl. Catal. B: Environ.* 306 (2022), 121098.
- [52] L.X. Song, H. Wang, S. Wang, Z.P. Qu, Dual-site activation of H<sub>2</sub> over Cu/ZnAl<sub>2</sub>O<sub>4</sub> boosting CO<sub>2</sub> hydrogenation to methanol, *Appl. Catal. B: Environ.* 322 (2023), 122137.
- [53] F.C.F. Marcos, R.S. Alvim, L.L. Lin, L.E. Betancourt, D.D. Petrolini, S. D. Senanayake, R.M.B. Alves, J.M. Assaf, J.A. Rodriguez, R. Giudici, E.M. Assaf, The role of copper crystallization and segregation toward enhanced methanol synthesis via CO<sub>2</sub> hydrogenation over CuZrO<sub>2</sub> catalysts: a combined experimental and computational study, *Chem. Eng. J.* 452 (2023), 139519.
- [54] A. Arandia, J.H. Yim, H. Warraich, E. Leppäkangas, R. Bes, A. Lempelto, L. Gell, H. Jiang, K. Meinander, T. Viinikainen, S. Huotari, K. Honkala, R.L. Puurunen, Effect of atomic layer deposited zinc promoter on the activity of copper-on-zirconia catalysts in the hydrogenation of carbon dioxide to methanol, *Appl. Catal. B: Environ.* 321 (2023), 122046.
- [55] C. Quilis, N. Mota, B. Pawelec, E. Millán, R.M. Navarro Yerga, Intermetallic PdZn/TiO<sub>2</sub> catalysts for methanol production from CO<sub>2</sub> hydrogenation: the effect of ZnO loading on PdZn-ZnO sites and its influence on activity, *Appl. Catal. B: Environ.* 321 (2023), 122064.
- [56] W.W. Wang, Z.P. Qu, L.X. Song, Q. Fu, Probing into the multifunctional role of copper species and reaction pathway on copper-cerium-zirconium catalysts for CO<sub>2</sub> hydrogenation to methanol using high pressure in situ DRIFTS, *J. Catal.* 382 (2020) 129–140.
- [57] W.G. Cui, Y.T. Li, L. Yu, H.B. Zhang, T.L. Hu, Zeolite-encapsulated ultrasmall Cu/ZnO<sub>x</sub> nanoparticles for the hydrogenation of CO<sub>2</sub> to methanol, *ACS Appl. Mater. Interfaces* 13 (2021) 18693–18703.
- [58] L.L. Ling, W. Yang, P. Yan, M. Wang, H.L. Jiang, Light-assisted CO<sub>2</sub> hydrogenation over Pd<sub>3</sub>Cu@UiO-66 promoted by active sites in close proximity, *Angew. Chem. Int. Ed.* (2021), 16396.
- [59] F. Marcos, F.M. Cavalcanti, D.D. Petrolini, L. Lin, E.M. Assaf, Effect of operating parameters on H<sub>2</sub>/CO<sub>2</sub> conversion to methanol over Cu-Zn oxide supported on ZrO<sub>2</sub> polymorph catalysts: characterization and kinetics, *Chem. Eng. J.* 427 (2022), 130947.